Probing the Formation of Cathode-Electrolyte Interface on Lithium Iron Phosphate Cathodes via In Operando Mechanical Measurements

Batuhan Bal[1,*], Bertan Ozdogru[1,*], Dan Thien Nguyen[2,3], Zheng Li[3,4], Vijayakumar Murugesan[2,3], Ömer Özgür Çapraz[1]

1) The School of Chemical Engineering, Oklahoma State University, Stillwater, OK 74078
2) Physical and Computational Sciences Directorate, Pacific Northwest National Laboratory, Richland, Washington 99352, United States
3) Joint Center for Energy Storage Research (JCESR), Lemont, Illinois 60439, United States
4) Davidson School of Chemical Engineering, Purdue University, West Lafayette, IN, 47907 USA

*Equal Contribution.

Abstract

Interfacial instabilities in electrodes control the performance and lifetime of Li-ion batteries. While the formation of solid-electrolyte interface (SEI) on anodes has received much attention, there is still lack of understanding about the formation of cathode-electrolyte interface (CEI) on the cathodes. To fill this gap, we report on dynamic deformations on lithium iron phosphate, $LiFePO_4$ cathodes during charge / discharge by utilizing in-operando digital image correlation, impedance spectroscopy and Cryo X-ray photoelectron spectroscopy. $LiFePO_4$ cathodes were cycled in either $LiPF_6$, $LiClO_4$ or LiTFSI- containing organic liquid electrolytes. Beyond the first cycle, Li-ion intercalation results in a nearly linear correlation between electrochemical strains and the state of (dis)-charge, regardless of the electrolyte chemistry. However, during the first charge in $LiPF_6$ -containing electrolyte, there is a distinct irreversible positive strain evolution at the onset of anodic current rise as well as current decay at around 4.0V. Impedance studies show the increase in surface resistance in the same potential window, suggesting the formation of CEI layers on the cathode. The chemistry of the CEI layer was characterized by X-ray photoelectron spectroscopy. LiF is detected in CEI layer starting as early as 3.4 V and $Li_xPO_yF_z$ appeared at voltages higher than 4.0 V during the first charge. Our approach offers new insights into the formation mechanism of CEI layers on the cathode electrodes, which is crucial for the development of robust cathode and electrolyte chemistries for higher performance batteries.

Key words: Cathode-electrolyte interface, strain, digital image correlation, X-ray photoelectron spectroscopy, Li-ion batteries

1. INTRODUCTION

Rechargeable Li-ion batteries have been widely used in daily life for a variety of applications including portable electronics, electrical vehicles and utility-scale storage.[1] When considering growing electrification efforts to mitigate dependance on fossil fuels, it becomes vital to further increase the cycle life of Li-ion batteries.[2] Capacity fade in Li-ion batteries is associated with the chemo-mechanical instabilities in electrodes such as mechanical deformations[3–6] and instabilities at electrode-electrolyte interface.[7–10] Repeated Li extraction / removal from the electrode results in electrochemical strain and stress generation, which eventually leads to particle fracture.[11] Electrode and electrolytes in Li-ion batteries operate outside of their thermodynamic stability windows, resulting in the formation of solid-electrolyte interface (SEI) on anodes and cathode-electrolyte interface (CEI) on cathodes.[12] Intrinsic properties of SEI / CEI layers impact the solvation mechanisms, Li-ion transport, and mechanical stability of the electrodes.[13]

An ideal SEI/CEI layer should provide effective Li^+ ion transport while being electronically insulating.[14,15] CEI layer should also mitigate undesired dissolution of transition metals from the cathode electrodes.[16,17] Furthermore, mechanical properties of SEI/CEI layers should be elastic enough to accommodate large volumetric changes in the electrode particles upon Li insertion and removal.[18,19] It is crucial to understand the formation mechanism of SEI / CEI layers and their impact on the performance of Li-ion batteries. The formation of solid-electrolyte interface on anodes has received much attention in the literature.[20] However, despite some efforts on identifying the structure and chemistry of CEI layers, the formation mechanism of CEI layers on the cathodes is still under debate. The lack of understanding about the formation mechanisms of CEI and its mechanical properties limits development of holistic approaches to further improve battery performance. Probing the formation of CEI while operating Li-ion batteries in typical conditions is needed to elucidate its complex mechanisms.

To date, most of the CEI studies are conducted via post-mortem analysis. Chemical composition of the CEI layers has been identified by X-ray photoelectron spectroscopy (XPS) [21,22] and Fourier transform infrared.[23] Morphological evolution of the CEI layers was tracked via cryogenic electron microscopy[24] and transmission electron microscopy.[25] Probing the CEI formation is challenging due to nanoscale-level CEI dimensions, complex cathode morphology, air/moisture/beam sensitivity. There are growing efforts to develop non- destructive situ / operando measurement capabilities to monitor and characterize the formation of CEI layers. [15,26–28] Differential electrochemical mass spectroscopy detects gas evolution[29,30], impedance spectroscopy is capable of monitoring resistance of the electrode[31,32], atomic force microscopy detects the morphological evolution in the film[33,34], X-ray absorption spectroscopy provides information about reaction intermediates[35,36] , and neutron diffractometry characterizes the structure of CEI layers.[37–39] However, these in situ / operando measurements are challenged by either extreme complexity, limitations in sample preparation, or difficult cell design.

In this study, we develop a non-destructive, in operando and optical method to probe dynamic changes on the composite cathode electrodes by utilizing digital image correlation (DIC) coupled with cryogenic XPS. DIC has been employed to study mechanical deformations in battery electrodes associated with phase transformation and interfacial instabilities.[40–43] Here, we utilized

the technique to probe the formation of CEI layers on lithium iron phosphate cathodes ($LiFePO_4$, LFP). LFP is chosen as a model cathode system due to its well-known two-phase reactions between (olivine phase) $LiFePO_4$ and (trigonal phase) $FePO_4$.[44–46] Electrochemical strain evolution is monitored while cycling the cathode in either $LiClO_4$, LiTFSI, or $LiPF_6$ salt-containing electrolyte chemistries. Beyond the first cycle, a linear relationship was observed between electrochemical strains and (dis)-charge capacities. Strain derivative calculations pointed out the phase transformation-induced electrochemical strains in the electrode. However, an abnormal electrochemical strain evolution was observed during the first cycle, more specifically the first charge in $LiPF_6$-containing batteries. Change in the electrode resistance was measured via electrochemical impedance spectroscopy and chemical composition of the CEI layers was identified via cryogenic XPS. The combination of in operando DIC with cryogenic XPS presents a landscape to probe dynamic changes on the cathode electrodes while providing mechanical and chemical properties of the CEI layers.

2. RESULTS AND DISCUSSION

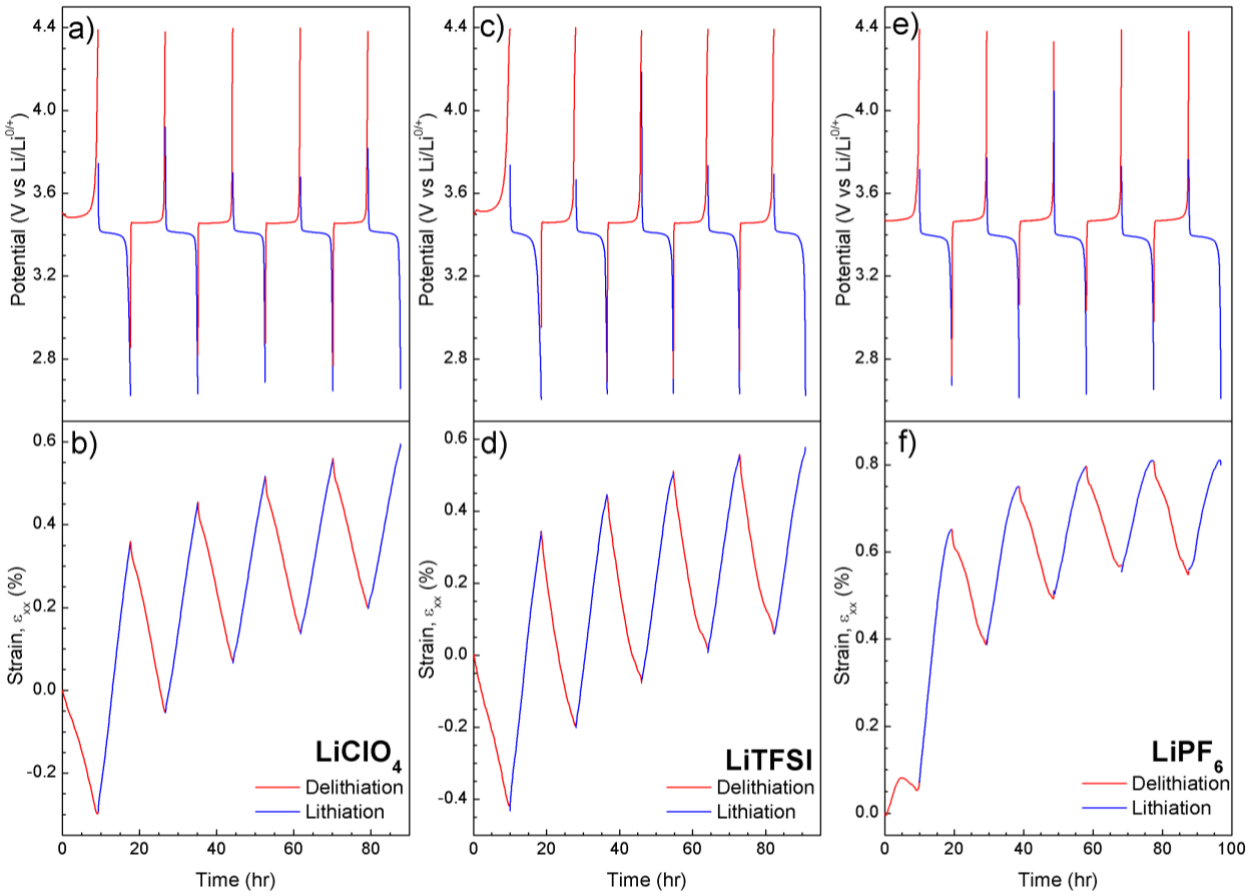

Figure 1: Strain generation in $LiFePO_4$ electrodes in different electrolyte salts during the 5 cycles at C/10 rate.

Probing mechanical deformations in $LiFePO_4$ cathodes in different electrolyte chemistries: Digital image correlation was utilized to monitor in operando strain generation in the $LiFePO_4$ cathode via galvanostatic cycle at C/10 in different electrolytes. Figure 1a shows potential and strain evolution in the electrode 1 M $LiClO_4$ in EC:DMC electrolyte. A single potential plateau at 3.49 and 3.41 V were observed during the delithiation and lithiation processes, respectively. These potential plateaus are associated with two phase reactions between (olivine phase) $LiFePO_4$ and (trigonal phase) $FePO_4$.[44–46] The overpotential was calculated by taking the difference of potential plateau values between charge and discharge cycles, and it was about 0.08, 0.05 and 0.05 V at the first, third and fifth cycle, respectively. The capacity of the electrode at 5th discharge cycle is 169 mAh/g, which is in good agreement with the theoretical capacity of $LiFePO_4$ cathode.[50] The associated mechanical behavior of the electrode is shown in Figure 1B. During the first delithiation, there is a generation of -0.29 % strains due to extraction of Li from the electrode structure. During lithiation, the insertion of Li^+ ions into electrode results in volumetric expansion. By the end of the first cycle, there is an irreversible strain of about 0.36 %.

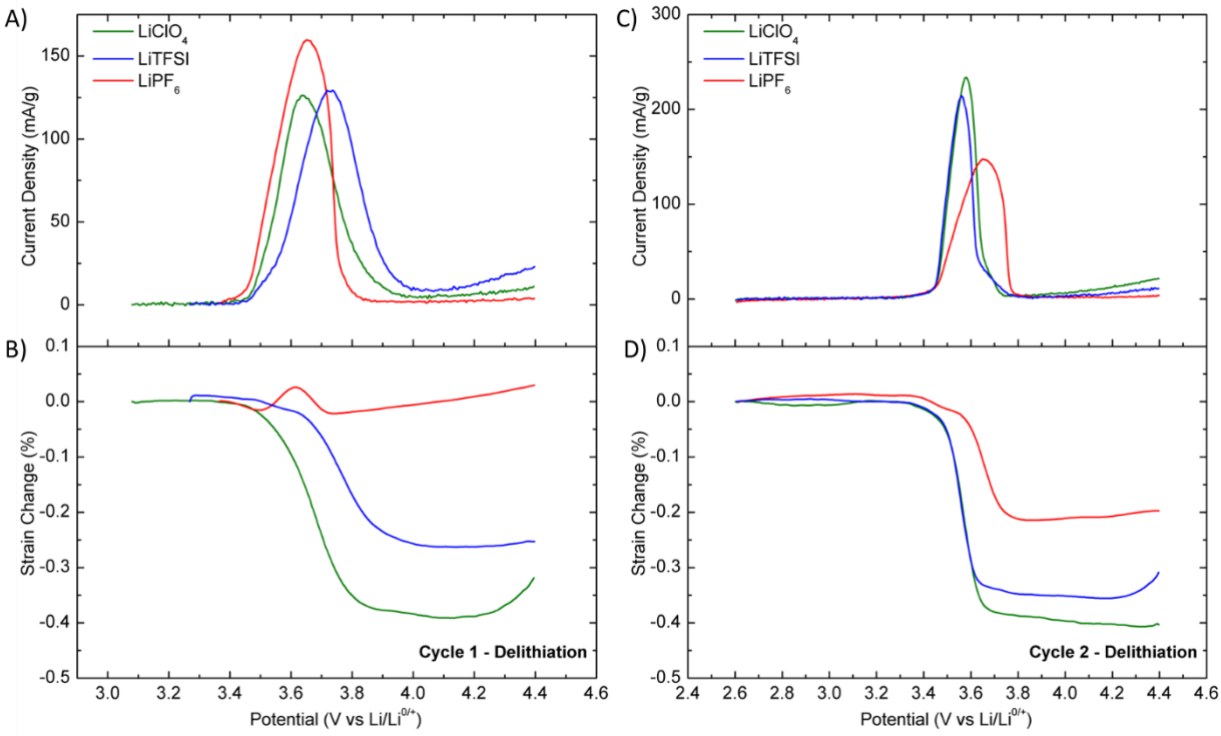

Figure 2: Strain and strain derivatives of $LiFePO_4$ electrodes in different electrolyte salts containing electrolyte solution for the first (A, B) and the second (C, D) charges at 50 µV/sec scan rate.

$LiFePO_4$ cathodes were also cycled in electrolytes containing LiTFSI and $LiPF_6$ salts in order to investigate the impact of electrolyte chemistry on the mechanical deformations. A single potential plateau is observed during charge and discharge reactions when the cathode was cycled in electrolytes containing LiTFSI or $LiPF_6$ salts. Associated mechanical behaviors of the electrode when cycled in LiTFSI or $LiPF_6$ salts containing electrolytes are shown at Figure 1d and 1f, respectively. As expected, the electrode undergoes volumetric expansions and shrinkage during

lithiation and delithiation cycles in LiTFSI-containing electrolytes, respectively. On the other hand, LFP electrodes demonstrated unexpected mechanical behavior during the first delithiation when cycled in $LiPF_6$-containing electrolyte solution (Figure 1f). Surprisingly, the electrode experiences about 0.08% expansions during the initial stages of the first delithiation even though Li ions were extracted from the structure. A single potential plateau at about 3.48 V in $LiPF_6$-containing electrolyte indicates the expected electrochemical response for the phase transition of the electrode during delithiation. Beyond the first delithiation, the mechanical response of the LFP electrode was as expected since the strains increased and decreased during the subsequent discharge and charge cycles, respectively. We suspect that the peculiar mechanical behavior of the electrode during the first delithiation in $LiPF_6$-containing electrolyte may be associated with the formation of the cathode-electrolyte interface (CEI) layers.

To further investigate the impact of electrolyte chemistry on the mechanical deformation, LFP cathodes were also charged / discharged via cyclic voltammetry while monitoring in operando strains generation in the electrode. Figure 2 shows the current generation and associated strains in the LFP electrodes cycled in different electrolyte solutions during the first and the second delithiation cycles. The current density in the LFP electrodes showed a distinct single peak which corresponds to the phase transformation from $LiFePO_4$ to $FePO_4$ in each electrolyte solution (Figure 2A and C). The current peaks were located at 3.64, 3.65, and 3.73 V for the $LiClO_4$, $LiPF_6$, and LiTFSI-based electrolyte solutions, respectively, during the first delithiation. In the second delithiation cycle, the current peaks were broader when the electrode was cycled in $LiPF_6$-containing electrolyte, compared to the other electrolyte chemistries. The electrochemical behavior of the LFP electrode at later cycles in different electrolyte chemistries is plotted in Supp. Figure S1. Overall, the evolution of current was broader when the electrode was cycled in $LiPF_6$-containing electrolyte. Broader current peak indicates the greater surface resistance towards the electrochemical reactions at the electrode / electrolyte interface.[49]

The associated mechanical behavior of the electrode during cyclic voltammetry is shown in Figure 2 B and D, respectively. Strain values were set to zero at the beginning of each lithiation and delithiation cycle in order to compare mechanical deformations in each charge / discharge process. When cycled in $LiClO_4$ or LiTFSI-containing electrolytes, the volume of the electrode contracted by -0.32% or -0.25% by the end of the first delithiation, respectively. Similar mechanical response of the electrode is also observed during the subsequent delithiation cycles (Figure 2D and Supp. Figure S1). On the other hand, when the electrode was cycled in $LiPF_6$-containing electrolyte, the electrode experienced 0.025% expansion starting from 3.6 V which coincides with the onset of the current generation during the first delithiation. As voltage increases to 3.6 V, the strain starts to decrease from 0.02 to -0.02 % until voltages reach 3.72 V for $LiPF_6$ salt containing electrolyte. Beyond the first delithiation, the behavior of the strain generations in the electrode were as expected in terms of increase and decrease in strains as a result of lithiation and delithiation, respectively in $LiPF_6$-containing electrolyte. Overall, the LFP electrode demonstrated unexpected mechanical deformation in $LiPF_6$-containing electrolyte when it was charged for the first time either via cyclic voltammetry or galvanostatic cycling.

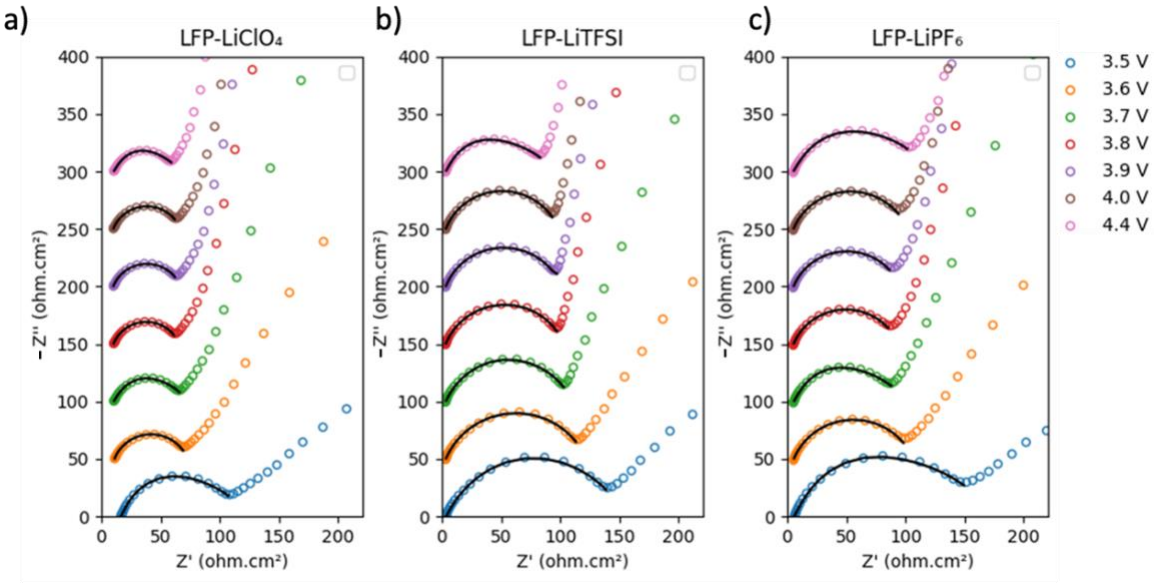

Figure 3: Nyquist curves obtained from different electrolyte salts-containing battery systems during the first charge at different voltages.

The evolution of interfacial resistance in the electrodes at different voltages during the first delithiation was investigated by conducting a series of impedance spectroscopy measurements. Formation of CEI layers is known to contribute to changes in the surface resistance and transport limitations. Previous studies showed CEI/SEI layer formation on the electrode surface which mostly causes additional resistance in batteries. [49,51,52] Electrochemical impedance spectroscopy (EIS) analyses were performed at different voltage values from 3.5 to 4.4 V during the first charge. Figure 3 depicts the Nyquist curves and their fits for different electrolyte salt-containing systems during the first charge. The surface resistances were evaluated using R_{ohmic} + $R_{surface}/Q_{surface}$ model to fit Nyquist plots, in which one semicircle and a Warburg element were observed.[53] The first intercept with the x-axis in the Nyquist plots is corresponding to ohmic resistance which is supposed to be almost identical for each voltage value along different electrolyte salts. Both CEI and SEI layer formation can be depicted via EIS, thus electrochemical interaction between positive and negative electrodes cannot be neglected in battery systems [54,55] . The first semicircles in our results were attributed to the sum of charge transfer resistance, LFP/Al interlayer, and CEI layer formation which is represented as surface resistance ($R_{surface}$). [49] Fittings applied only on the semicircles due to the Warburg element is corresponding to Li^+ diffusion into solid-phase electrode.[56] Decrease in first semicircle sizes of both $LiClO_4$ and LiTFSI salts containing systems is visible when voltage values increase (Figure 3a-b). However, only the $LiPF_6$-containing system showed a rise in surface resistance values after 3.7 V (Figure 3c). Interestingly, it also coincides with the increase in positive strains (Figure 2). The correlation between increase in the thickness of CEI layer and resistance was previously reported for NMC cathodes. [57] Formation of the CEI layers would lead to increase in the average particle volume in the composite electrode, which translates into the irreversible strain evolution in the composite electrode.

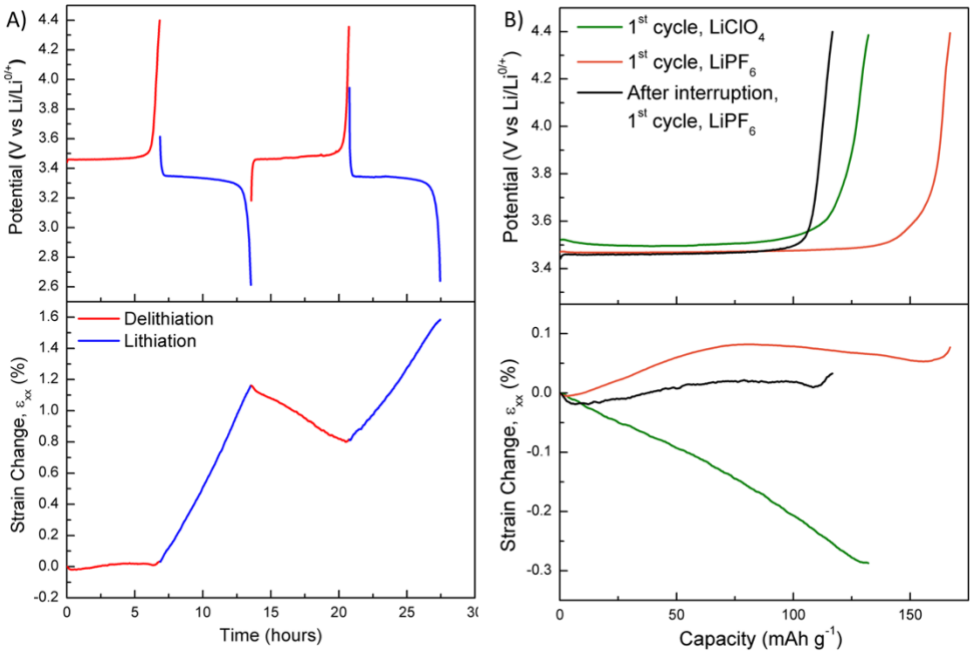

Figure 4: A) Strain change of the interrupted $LiFePO_4$ electrodes in $LiPF_6$ in EC:DMC and B) strain change difference of the $LiFePO_4$ electrodes in various electrolyte salts solutions before and after interruption experiments

Control experiments were conducted to further verify the relationship between instabilities of $LiPF_6$-containing electrolyte and irreversible mechanical deformations in the electrode during the first delithiation. We hypothesized that the decomposition of $LiPF_6$-containing electrolyte is responsible for the positive strain evolution during delithiation. To test the hypothesis, LFP electrode was charged and discharged for one cycle in the $LiClO_4$-containing electrolyte for the control experiment. Then, electrochemical cycling was interrupted, the electrode was washed with EC:DMC solvent, and the electrolyte in the custom cell was switched with $LiPF_6$-containing electrolyte. Afterwards, the electrode was charged and discharged in $LiPF_6$-containing electrolyte (Figure 4A). Single potential plateaus were recorded at 3.46 and 3.35 V during charge and discharge. After the interruption and switching to $LiPF_6$-containing electrolyte, electrochemical strains were almost zero during the first delithiation even though lithium was removed from the electrode structure. In the subsequent cycles, the electrochemical strains increased and decreased during lithiation and delithiation processes as expected, respectively. Figure 4B was plotted to visualize the strain evolution in the electrode when cycled in either $LiPF_6$ or $LiClO_4$-containing electrolyte for the first time. The control experiment suggests the electrolyte decomposition in $LiFePO_4$-containing electrolytes may contribute to the formation of cathode-electrolyte interface (CEI) and overall expansions in the volume of the electrode during the first delithiation.

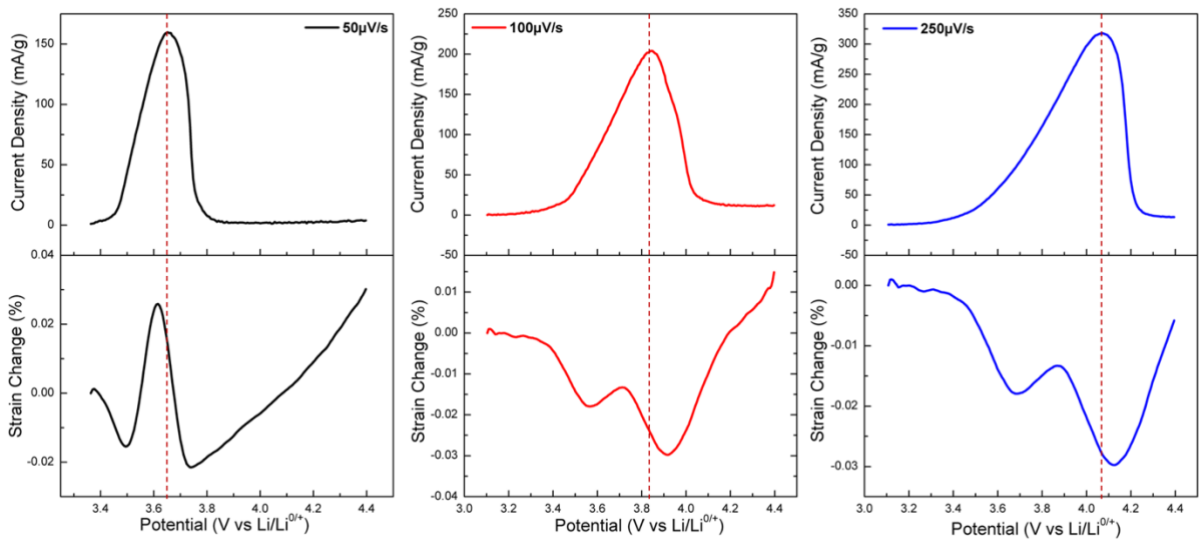

Figure 5: Current evolutions and strain changes of the $LiFePO_4$ electrodes at different scan rates during first and second delithiation.

Kinetic behavior for the decomposition of $LiPF_6$-containing electrolyte was further investigated by cycling electrodes in $LiPF_6$-containing electrolyte at different scan rates via cyclic voltammetry. Figure 5 shows the current and strain evolution at different rates for the first delithiation. The current and strains evolution for the subsequent lithiation and delithiation cycles were plotted in Supp. Figure S2. As expected, redox potentials at different scan rates slightly shift through higher voltages due to the kinetic limitations for phase transformation at faster scan rates.[58] The overpotential of the LFP electrodes were calculated based on the difference between the location of the anodic and cathodic peaks and it was 0.43, 0.76 and 1.22 V 50, 100 and 250 μV/sec scan rates, respectively. The associated strain evolution during the first delithiation demonstrated similar behavior in all scan rates. Overall, negative strains were generated initially, followed by the increase until about where the current reaches its maximum value. Then, there is reduction in strains until current becomes almost zero. At higher voltages, strain starts to increase even though current was negligible. Additionally, the different scan rate effect is clearly noticeable in mechanical behavior in which strain values are 0.03, 0.01, and -0.005 at 50, 100, 250 μV/sec, respectively. The SEI layer formation was explained by proposing parabolic oxidation law and proposed as time-dependent growth without cycle count dependence.[59] Furthermore, there have been reports about the dependance of cycle time and CEI/SEI layer thickness in the literature.[55,59,60] Our previous studies also demonstrated that the formation of the SEI/CEI layers could contribute to the irreversible strain generation in the electrode.[40,43,61] These studies also pointed out a time-dependent irreversible deformation in electrodes associated with the SEI/CEI layer formation.

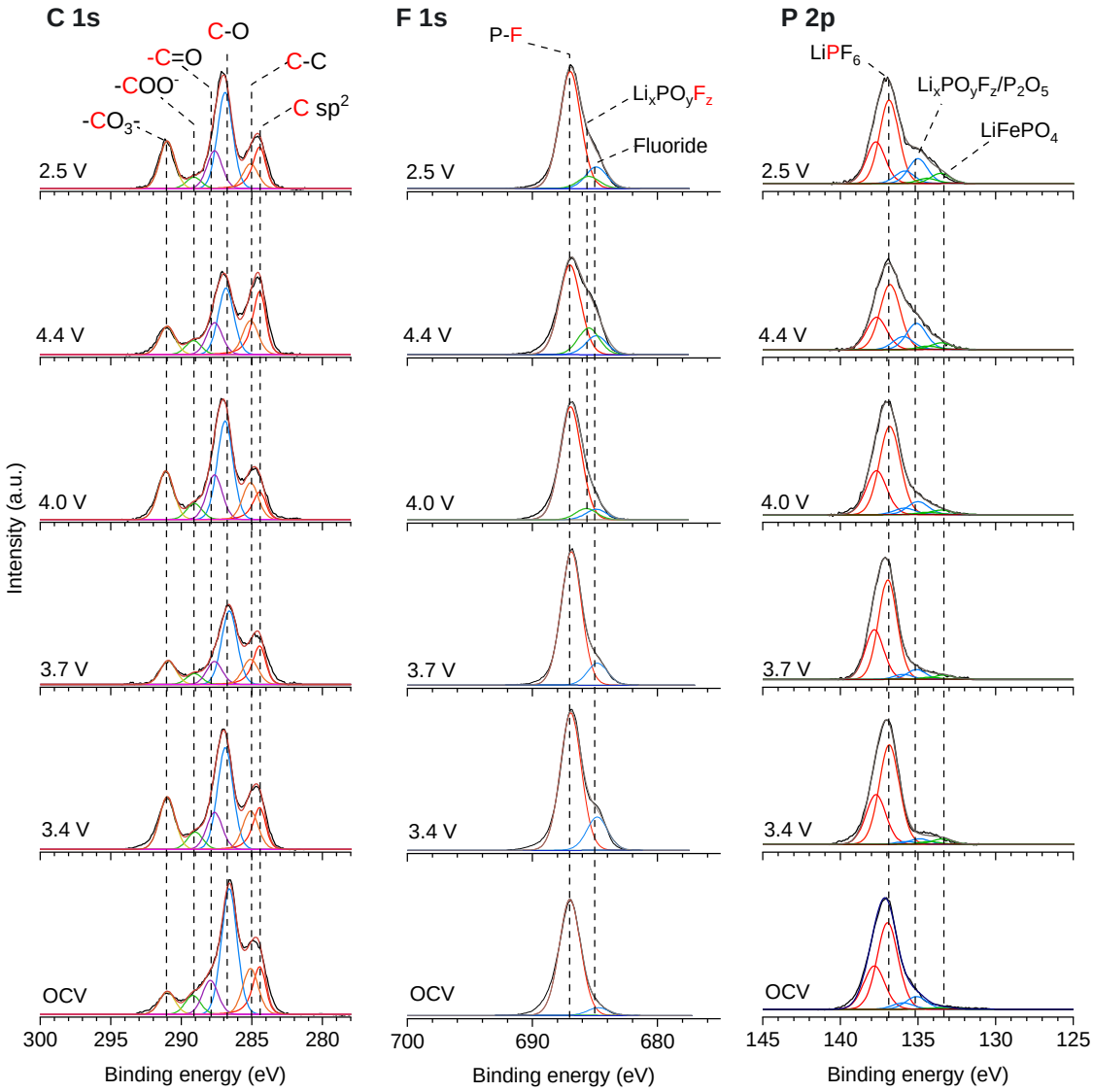

Figure 6: Cryo XPS analysis of LFP cathode during initial cycles collected at OCV, 3.4V, 3.7 V, 4.0 V, 4.4 V, and after first discharge (2.5 V). The spectra were collected at the same position and with minimum scans to avoid the X-ray beam damage of electrode and electrolyte.

The chemistry of CEI layers on the LFP cathodes cycled in $LiPF_6$-containing electrolytes was investigated by performing cryogenic X-ray photoelectron microscopy (XPS) measurements (Figure 6). At OCV, the C 1s spectrum of LFP cathode shows signals of alkyl carbonates at 291.7 eV (-CO_3-) and 287.7 eV (C-O), C-C (285 eV), and CMC binder such at 285.8 eV (C-O), 287 eV(C=O), 289.1 eV (COO-), and carbon black (284.5 eV). There is also appearance of CO_3-detected at ~291 eV. In the F 1s spectrum, the main signal at 687 eV is attributed to $LiPF_6$.[62] The P 2p spectrum consists of a strong signal of $2p_{3/2}$ (137.5 eV) and $2p_{1/2}$ doublet.[63] A small signal in the lower binding energy of near 135 eV is assigned to P_2O_5 (135.4 eV), which is probably due to surface oxidation of the LFP cathode during preparation and storage.[63]

The electrode was charged and discharged via cyclic voltammetry until the charge potentials of 3.4 V, 3.7 V, 4.0 V, 4.4 V and discharge potential of 2.5 V. The oxidation of electrolytes containing $LiPF_6$ salt dissolved in carbonate solvents were reported to as low as 3.3 V *vs.* $Li^{0/+}$ on metals.[65] A strong signal of LiF was also observed at 685 eV.[62,66] The P 2p spectrum showed an enhanced signal at 136.4 eV from P_2O_5 and/or $Li_xPO_yF_z$. This result suggests the decomposition of $LiPF_6$ and associated formation of CEI layers occurred as early as 3.4 V *vs.* Li/Li^+. This data is consistent with the change of strain in electrode that occurred near 3.4 V during the first charge (Figure 5). At the higher voltages (> 4.0V), the signal of $Li_xPO_yF_z$ was clearly observed in the F 1s spectra, which is consistent with the strengthening of the P 2p signal observed near 135 eV. In the following step of charging and discharging, the signals gradually increase, which implies the growth of CEI during the initial cycle. These fluorinated inorganic species are reported to originate from the decomposition of the $LiPF_6$ salt by the following reactions:[64,65,67]

$$LiPF_6\ (sol.) \leftrightarrow LiF\ (s) + PF_5\ (sol.) \qquad \text{[Eqn. 1]}$$

$$PF_5\ (sol.) + H_2O\ (trace) \rightarrow POF_3\ (sol.) + HF(sol.) \qquad \text{[Eqn. 2]}$$

$$POF_3\ (sol.) + Li_2O\ (s) \rightarrow LiF\ (s) + Li_xPO_yF_z\ (s) \qquad \text{[Eqn. 3]}$$

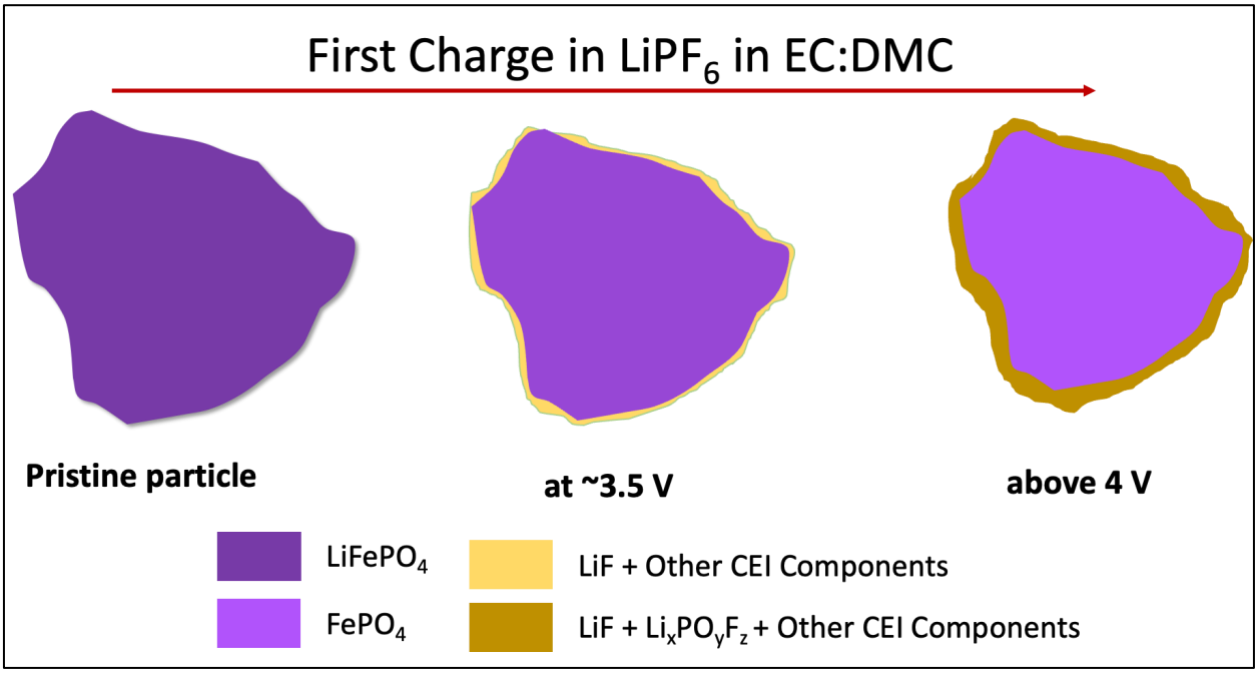

Figure 7: Proposed CEI layer evolution mechanism for LFP electrodes in 1 M $LiPF_6$ in EC:DMC.

The proposed mechanism behind the irreversible deformations during the first charge was depicted in Figure 7. In this work, irreversible positive strain generation in the $LiFePO_4$ electrode suggests the decomposition of the electrolyte species on the electrode surface during the first charge in $LiPF_6$-containing electrolytes (Figure 1-2). Beyond the first charge, the electrode demonstrates a linear relationship between electrochemical strain and (dis)-charge capacities, regardless of the electrolyte chemistry (Supp. Figure S4). A linear relationship between strain and capacities indicates the intercalation-induced deformations at the later cycles. Previous digital image correlation studies also demonstrated the similar phenomena between the formation of positive irreversible strains and the formation of SEI on graphite anode[40] and $LiMn_2O_4$ cathodes.[68] The increase in the surface resistance in $LiPF_6$-containing electrolyte further suggests the formation of CEI layers on the $LiFePO_4$ electrode (Figure 3). The correlation between CEI-induced strains and impedance was reported for $LiMn_2O_4$ cathodes previously.[68] Strain measurements during cyclic voltammetry presents an interesting fact about the initiation of the positive strains during the first charge. Strains were almost negligible until about a potential where anodic current begins to rise (Figure 5). Around the similar potentials, XPS measurements indicated chemical species on the electrode surface due to the oxidation of ethylene carbonate solvent as well as the formation of LiF due to hydrolysis of the $LiPF_6$ salt [Eqn 1]. Trace amounts of residual water react with the side product of PF_5 to form POF_3 and HF species [Eqn 2]. The residual water on the battery materials exists due to persistent adsorbed water on the electrode surface.[69] The reaction between POF_3 and Li_2O leads to formation of $Li_xPO_yF_z$ on the electrode surface [Eqn 3]. Therefore, the formation of LiF and the following $Li_xPO_yF_z$ involves the series of reactions including electrochemical oxidation and chemical reactions. Cyclic voltammetry at different rates indicates that onset of the positive takes place at different potentials. Instead, the formation of positive strains at higher potentials coincides with the decay of the anodic current. The negligible current at these potentials suggests the completion of the delithiation process, therefore there is no longer (negative) strain generation in the electrode associated with the extraction of Li ions. The increase in the strains at this point is associated with the continuation of the CEI formation during the later stages of first charge.

3. CONCLUSION

Understanding CEI layer formation is beneficial to improve battery life by tailoring desired interphases between electrodes and electrolytes. However, it is challenging to probe the formation dynamics of CEI layers due to lack of in operando capabilities. In this work, we utilized in operando digital image correlation technique to understand the formation mechanisms of CEI layers on $LiFePO_4$ cathodes. The cathodes were cycled in either $LiPF_6$, $LiClO_4$ or LiTFSI-containing electrolytes via galvanostatic cycle and cyclic voltammetry at different rates. Mechanical measurements detected irreversible positive strain generation in the electrode, only during the first charge in $LiPF_6$-containing electrolyte. Control experiments further indicated the relationship between the irreversible strains and the instabilities in the $LiPF_6$-containing electrolyte. Impedance measurements demonstrated an increase in surface resistance when the electrode cycled in $LiPF_6$-containing electrolytes during the first charge. Strain data acquired at

different cyclic rates indicates the generation of possible strains at a lower potential (about 3.5V) where anodic current began to rise as well as at higher potentials (>4.0 V) where anodic current becomes almost negligible. Cryogenic X-ray photoelectron microscopy measurements indicated the formation of LiF at a lower potential, followed by the formation of $Li_xPO_yF_z$ at higher potentials. Our study showed that the formation of CEI layers on the electrodes leaves unique mechanical fingerprints, which can be utilized to understand the decomposition of electrolyte species on the electrodes. In the future, we will apply in operando mechanical measurements to understand the formation mechanisms of CEI layers on Na-ion batteries cathodes.

4. EXPERIMENTAL SECTION

Electrode Fabrication: The carboxymethyl cellulose (CMC) was dissolved in ultrapure water and mixed using a centrifugal mixer. Electrode slurries were prepared by mixing $LiFePO_4$ powders, carboxymethyl cellulose (CMC, average MW ~ 700,000, Aldrich) as a binder, Super P as a conductive carbon in the weight ratio of 8:1:1 using Twinky mixer. $LiFePO_4$ composite electrodes were fabricated by blade casting the slurry on an aluminum foil (15 μm thick, MTI). The electrode was dried in room temperature. The electrodes were punched using quarter inch punches to obtain round shaped electrodes for the coin cells studies. For strain measurements, once dried, the composite electrode was peeled off from aluminum foil and cut into a rectangular shape that was appropriate for the custom strain cells.[47–49]

Electrochemical Investigation: The fabricated free standing rectangular-shaped $LiFePO_4$ composite electrodes were characterized using galvanostatic and cyclic voltammetry tests. Galvanostatic cycles were performed at C/10 discharge rate. Different electrolyte chemistries were prepared by dissolving 1 M $LiClO_4$, $LiPF_6$ or LiTFSI in 1:1 (V:V) ethylene carbonate (EC, anhydrous, 99%, Sigma Aldrich) : dimethyl carbonate (DMC, anhydrous, >99%, Sigma Aldrich). In this work, cyclic voltammetry was conducted in different electrolyte solutions at 50, 100, and 250 μV/sec between 2.5 V to 4.4 V.

Strain Measurements: A custom cell design was preferred for the strain measurements of the LFP electrodes. The custom cells were assembled using a polychlorotrifluoroethylene (PCTFE, Plastics International) framework in which there was a stainless-steel sample holder for both counter and working electrodes. To observe mechanical changes in the composite electrodes, a quartz window (99.995% SiO2, 1/16 in thick, 2 in diameter, McMaster-Carr) was placed onto the top of the custom cell and the leakage-free assembly was achieved by placing the Viton O-rings (Grainger) and a stainless-steel flange. A detailed description of the custom cell was provided in the previous works.[47–49] Optical investigation of the LFP electrodes occurred using the digital image correlation (DIC) technique with a Grasshopper3 5.0 MP camera (Sony IMX250, resolution, 2448 (w)*2048(h) pixel) that is attached with 12.0× adjustable zoom lens (NAVITAR) for an effective resolution of 0.873 μm/pixel. A LED light source was directed onto the LFP electrodes to achieve visible speckle patterns. During the galvanostatic cycling of the electrodes, images were captured every 10 and 2 minutes for open circuit potential measurements and at C/10 rate,

respectively. Image capturing times were selected as 0.5, 1, and 2 minutes for cyclic voltammetry at 50, 100, 250 µV/sec scan rates, respectively.

Electrochemical Impedance Spectroscopy: Surface resistance investigation of the LFP electrodes was performed on coin cells via electrochemical impedance spectroscopy (EIS, Biologic SP-150) using two electrode measurements. EIS measurements were performed at room temperature, using an excitation voltage of 10 mV, at the frequency range of 500 kHz – 50 mHz for pristine electrodes at open circuit potential. After performing the first EIS at open circuit voltage, a voltage staircase experiment was performed using an intermitted 0.1 V voltage step between 3.5 – 4.0 and, at 4.4 V with a scan rate 50 µV/s for EIS measurements. The voltage staircase experiments were applied to different electrolyte solutions containing coin cells to investigate the electrolyte solution effect on the surface resistance of the LFP electrodes. Furthermore, the obtained Nyquist curves for the different coin cells were fitted using $R_{ohmic}+Q_{surface}/R_{surface}$ equivalent circuit model by EC-Lab, Z-fit software. CR2032 coin cells were assembled in which the LFP electrodes, Li foil (99.9% metal basis, Alfa Aesar) as a counter electrode, and Celgard polyethylene film as a separator exist. The 25 µL electrolyte solutions were dropped onto each layer using a pipet. Coin cell assembly and electrolyte preparation were performed in an argon-filled glovebox.

Cryo- X-ray photoelectron spectroscopy: The porous electrode was prepared by coating a slurry consisting of LFP, carbon black, and CMC binder at a weight ratio of 8:1:1, respectively onto Al mesh current collector (15 µm thick, MTI). The electrode was then dried in the vacuum and punched into 12.7 mm diameter dishes. The *in-situ* coin cell was constructed with the active material facing the open window of the coin cell can (Figure S5A). The coin cell was then rested for 12h before conducting electrochemical measurements. After resting, the coin cell was mounted on the sample holder as shown in Figure S5B. The temperature of the sample holder was then reduced to -130 °C for 20 minutes using a flow of liquid nitrogen in a loading chamber inside an Ar-filled glovebox (Figure S6). This step aims to convert liquid electrolyte into the solid state to avoid evaporation during transfer and XPS analysis. The loading chamber was then pumped down to the pressure of ~10^{-8} torr and the coin cell was transferred to *cryo*- stage inside the XPS analysis chamber. The temperature of the coin cell was maintained at -130 °C during XPS analysis. After each XPS analysis, the coin cell was transferred back to the cryo state loading chamber before warming up to room temperature inside the glovebox. The charging of the LFP cathode was conducted using linear sweep voltammetry between OCV to 4.4 V vs. Li/Li^+, followed by discharging to 2.5 V at a scan rate of 0.1 mV s^{-1}. XPS analysis was conducted at OCV, 3.4 V, 3.7 V, 4.0 V, 4.4V, and after 1 cycle (discharged to 2.5 V). XPS analysis was performed using a Kratos Axis Ultra DLD spectrometer, which consists of an Al Kα monochromatic X-ray source (1486.6 eV) and a high-resolution spherical mirror analyzer. X-ray source was operated at 150 W power and the emitted photoelectrons were collected at the analyzer entrance slit normal to the sample surface. The high-resolution spectra were collected at a pass energy of 40 eV with a step sized of 0.1 eV. The XPS measurement was conducted without applying charge neutralizer to avoid the decomposition of surface components. XPS data were analyzed using CasaXPS software. All the XPS peaks were charge referenced to F 1s spectra of $LiPF_6$ at 687.5 eV. The charge reference was

determined using cryogenic XPS of 1M $LiPF_6$ in EC/DMC (1:1, vol.) drop-casted on graphite electrode.

ACKNOWLEDGEMENT

All *in operando* strain and electrochemical measurements were carried out at Oklahoma State University and supported by the U.S. Department of Energy, Office of Science, Basic Energy Sciences (Award number DE-SC0021251). V.M., D. T. N., and Z. L. acknowledges funding as part of the Joint Center for Energy Storage Research, an Energy Innovation Hub funded by the U.S. Department of Energy, Office of Science, Basic Energy Science. Ö. Ö. Ç conceived the idea and supervised the work. B. B. and B. Ö. performed in situ strain measurements and data analysis. D. T. N. and Z. L. performed and analyzed XPS measurements. All authors discussed the results. The authors declare that they have no competing interests. All data needed to evaluate the conclusions in the paper are present in the paper and/or in the Supplementary Materials. Additional data related to this paper may be requested from the authors.

CONFLICT OF INTEREST

The authors declare that they have no conflict of interest.

REFERENCES

(1) Grey, C. P.; Hall, D. S. Prospects for Lithium-Ion Batteries and beyond—a 2030 Vision. *Nature Communications 2020 11:1* **2020**, *11* (1), 1–4. https://doi.org/10.1038/s41467-020-19991-4.

(2) Goodenough, J. B. Electrochemical Energy Storage in a Sustainable Modern Society. *Energy Environ Sci* **2013**, *7* (1), 14–18. https://doi.org/10.1039/C3EE42613K.

(3) Yan, P.; Zheng, J.; Gu, M.; Xiao, J.; Zhang, J. G.; Wang, C. M. Intragranular Cracking as a Critical Barrier for High-Voltage Usage of Layer-Structured Cathode for Lithium-Ion Batteries. *Nature Communications 2017 8:1* **2017**, *8* (1), 1–9. https://doi.org/10.1038/ncomms14101.

(4) Ryu, H. H.; Park, K. J.; Yoon, C. S.; Sun, Y. K. Capacity Fading of Ni-Rich Li[NixCoyMn1-x-y]O2 (0.6 ≤ x ≤ 0.95) Cathodes for High-Energy-Density Lithium-Ion Batteries: Bulk or Surface Degradation? *Chemistry of Materials* **2018**, *30* (3), 1155–1163. https://doi.org/10.1021/ACS.CHEMMATER.7B05269.

(5) Liu, H.; Wolf, M.; Karki, K.; Yu, Y. S.; Stach, E. A.; Cabana, J.; Chapman, K. W.; Chupas, P. J. Intergranular Cracking as a Major Cause of Long-Term Capacity Fading of Layered Cathodes. *Nano Lett* **2017**, *17* (6), 3452–3457. https://doi.org/10.1021/ACS.NANOLETT.7B00379.

(6) Zhang, S. Chemomechanical Modeling of Lithiation-Induced Failure in High-Volume-Change Electrode Materials for Lithium Ion Batteries. *npj Computational Materials 2017 3:1* **2017**, *3* (1), 1–11. https://doi.org/10.1038/s41524-017-0009-z.

(7) Michan, A. L.; Divitini, G.; Pell, A. J.; Leskes, M.; Ducati, C.; Grey, C. P. Solid Electrolyte Interphase Growth and Capacity Loss in Silicon Electrodes. *J Am Chem Soc* **2016**, *138* (25), 7918–7931. https://doi.org/10.1021/JACS.6B02882.

(8) Wu, Y.; Liu, X.; Wang, L.; Feng, X.; Ren, D.; Li, Y.; Rui, X.; Wang, Y.; Han, X.; Xu, G. L.; Wang, H.; Lu, L.; He, X.; Amine, K.; Ouyang, M. Development of Cathode-Electrolyte-Interphase for Safer Lithium Batteries. *Energy Storage Mater* **2021**, *37*, 77–86. https://doi.org/10.1016/J.ENSM.2021.02.001.

(9) Wang, H.; Li, X.; Li, F.; Liu, X.; Yang, S.; Ma, J. Formation and Modification of Cathode Electrolyte Interphase: A Mini Review. *Electrochem commun* **2021**, *122*, 106870. https://doi.org/10.1016/J.ELECOM.2020.106870.

(10) Xu, K. Nonaqueous Liquid Electrolytes for Lithium-Based Rechargeable Batteries. *Chem Rev* **2004**, *104* (10), 4303–4417. https://pubs.acs.org/doi/10.1021/cr030203g.

(11) Li, P.; Zhao, Y.; Shen, Y.; Bo, S. H. Fracture Behavior in Battery Materials. *Journal of Physics: Energy* **2020**, *2* (2), 022002. https://doi.org/10.1088/2515-7655/AB83E1.

(12) Maier, J. Thermodynamics of Electrochemical Lithium Storage. *Angewandte Chemie International Edition* **2013**, *52* (19), 4998–5026. https://doi.org/10.1002/ANIE.201205569.

(13) Fu, W.; Kim, D.; Wang, F.; Yushin, G. Stabilizing Cathodes and Interphases for Next-Generation Li-Ion Batteries. *J Power Sources* **2023**, *561*, 232738. https://doi.org/10.1016/J.JPOWSOUR.2023.232738.

(14) Bai, P.; Ji, X.; Zhang, J.; Zhang, W.; Hou, S.; Su, H.; Li, M.; Deng, T.; Cao, L.; Liu, S.; He, X.; Xu, Y.; Wang, C. Formation of LiF-Rich Cathode-Electrolyte Interphase by Electrolyte Reduction. *Angewandte Chemie International Edition* **2022**, *61* (26), e202202731. https://doi.org/10.1002/ANIE.202202731.

(15) Sungjemmenla; Vineeth, S. K.; Soni, C. B.; Kumar, V.; Seh, Z. W. Understanding the Cathode–Electrolyte Interphase in Lithium-Ion Batteries. *Energy Technology* **2022**, *10* (9), 2200421. https://doi.org/10.1002/ENTE.202200421.

(16) Hestenes, J. C.; Sadowski, J. T.; May, R.; Marbella, L. E. Transition Metal Dissolution Mechanisms and Impacts on Electronic Conductivity in Composite LiNi0.5Mn1.5O4Cathode Films. *ACS Materials Au* **2022**, *3*. https://doi.org/10.1021/ACSMATERIALSAU.2C00060/

(17) Zhao, L.; Chénard, E.; Çapraz, Ö. Ö.; Sottos, N. R.; White, S. R. Direct Detection of Manganese Ions in Organic Electrolyte by UV-Vis Spectroscopy. *J Electrochem Soc* **2018**, *165* (2), A345–A348. https://doi.org/10.1149/2.1111802JES.

(18) Heng, S.; Shi, Q.; Wang, Y.; Qu, Q.; Zhang, J.; Zhu, G.; Zheng, H. In Situ Development of Elastic Solid Electrolyte Interphase via Nanoregulation and Self-Polymerization of Sodium

Itaconate on Graphite Surface. *ACS Appl Energy Mater* **2019**, *2* (2), 1336–1347. https://doi.org/10.1021/ACSAEM.8B01912.

(19) Wu, H.; Chan, G.; Choi, J. W.; Ryu, I.; Yao, Y.; Mcdowell, M. T.; Lee, S. W.; Jackson, A.; Yang, Y.; Hu, L.; Cui, Y. Stable Cycling of Double-Walled Silicon Nanotube Battery Anodes through Solid–Electrolyte Interphase Control. *Nature Nanotechnology 2012 7:5* **2012**, *7* (5), 310–315. https://doi.org/10.1038/nnano.2012.35.

(20) Michan, A. L.; Divitini, G.; Pell, A. J.; Leskes, M.; Ducati, C.; Grey, C. P. Solid Electrolyte Interphase Growth and Capacity Loss in Silicon Electrodes. *J Am Chem Soc* **2016**, *138* (25), 7918–7931. https://doi.org/10.1021/JACS.6B02882.

(21) Philippe, B.; Hahlin, M.; Edström, K.; Gustafsson, T.; Siegbahn, H.; Rensmo, H. Photoelectron Spectroscopy for Lithium Battery Interface Studies. *J Electrochem Soc* **2016**, *163* (2), A178–A191. https://doi.org/10.1149/2.0051602JES.

(22) Verma, P.; Maire, P.; Novák, P. A Review of the Features and Analyses of the Solid Electrolyte Interphase in Li-Ion Batteries. *Electrochim Acta* **2010**, *55* (22), 6332–6341. https://doi.org/10.1016/J.ELECTACTA.2010.05.072.

(23) Pérez-Villar, S.; Lanz, P.; Schneider, H.; Novák, P. Characterization of a Model Solid Electrolyte Interphase/Carbon Interface by Combined in Situ Raman/Fourier Transform Infrared Microscopy. *Electrochim Acta* **2013**, *106*, 506–515. https://doi.org/10.1016/J.ELECTACTA.2013.05.124.

(24) Zhang, Z.; Yang, J.; Huang, W.; Wang, H.; Zhou, W.; Li, Y.; Li, Y.; Xu, J.; Huang, W.; Chiu, W.; Cui, Y. Cathode-Electrolyte Interphase in Lithium Batteries Revealed by Cryogenic Electron Microscopy. *Matter* **2021**, *4* (1), 302–312. https://doi.org/10.1016/j.matt.2020.10.021.

(25) Wang, J.; Wang, D. Cryo-EM Reveals the Structure and Chemistry of the Silicon Solid-Electrolyte Interphase. *Chem* **2020**, *6* (2), 331–334. https://doi.org/10.1016/J.CHEMPR.2020.01.006.

(26) Novák, P.; Panitz, J. C.; Joho, F.; Lanz, M.; Imhof, R.; Coluccia, M. Advanced in Situ Methods for the Characterization of Practical Electrodes in Lithium-Ion Batteries. *J Power Sources* **2000**, *90* (1), 52–58. https://doi.org/10.1016/S0378-7753(00)00447-X.

(27) Amalraj, S. F.; Aurbach, D. The Use of in Situ Techniques in R&D of Li and Mg Rechargeable Batteries. *Journal of Solid State Electrochemistry* **2011**, *15* (5), 877–890. https://doi.org/10.1007/S10008-011-1324-9.

(28) Zampardi, G.; Mantia, F. La; Batteries,]; Reviews, S. Solid–Electrolyte Interphase at Positive Electrodes in High-Energy Li-Ion Batteries: Current Understanding and Analytical Tools. *Batter Supercaps* **2020**, *3* (8), 672–697. https://doi.org/10.1002/BATT.201900177.

(29) Sharon, D.; Hirsberg, D.; Salama, M.; Afri, M.; Frimer, A. A.; Noked, M.; Kwak, W.; Sun, Y. K.; Aurbach, D. Mechanistic Role of Li+ Dissociation Level in Aprotic Li-O2 Battery. *ACS Appl Mater Interfaces* **2016**, *8* (8), 5300–5307. https://doi.org/10.1021/ACSAMI.5B11483.

(30) Lin, C. F.; Kozen, A. C.; Noked, M.; Liu, C.; Rubloff, G. W. ALD Protection of Li-Metal Anode Surfaces – Quantifying and Preventing Chemical and Electrochemical Corrosion in Organic Solvent. *Adv Mater Interfaces* **2016**, *3* (21), 1600426. https://doi.org/10.1002/ADMI.201600426.

(31) Croce, F.; Nobili, F.; Deptula, A.; Lada, W.; Tossici, R.; D'Epifanio, A.; Scrosati, B.; Marassi, R. An Electrochemical Impedance Spectroscopic Study of the Transport Properties of LiNi0.75Co0.25O2. *Electrochem commun* **1999**, *1* (12), 605–608. https://doi.org/10.1016/S1388-2481(99)00123-X.

(32) Aurbach, D.; Gamolsky, K.; Markovsky, B.; Salitra, G.; Gofer, Y.; Heider, U.; Oesten, R.; Schmidt, M. The Study of Surface Phenomena Related to Electrochemical Lithium Intercalation into Li[Sub x]MO[Sub y] Host Materials (M = Ni, Mn). *J Electrochem Soc* **2000**, *147* (4), 1322. https://doi.org/10.1149/1.1393357.

(33) Kuznetsov, V.; Zinn, A. H.; Zampardi, G.; Borhani-Haghighi, S.; La Mantia, F.; Ludwig, A.; Schuhmann, W.; Ventosa, E. Wet Nanoindentation of the Solid Electrolyte Interphase on Thin Film Si Electrodes. *ACS Appl Mater Interfaces* **2015**, *7* (42), 23554–23563. https://doi.org/10.1021/ACSAMI.5B06700.

(34) Tokranov, A.; Sheldon, B. W.; Li, C.; Minne, S.; Xiao, X. In Situ Atomic Force Microscopy Study of Initial Solid Electrolyte Interphase Formation on Silicon Electrodes for Li-Ion Batteries. *ACS Appl Mater Interfaces* **2014**, *6* (9), 6672–6686. https://doi.org/10.1021/AM500363T.

(35) Shearing, P.; Wu, Y.; Harris, S. J.; Brandon, N. In Situ X-Ray Spectroscopy and Imaging of Battery Materials. *Electrochemical Society Interface* **2011**, *20* (3), 43–47. https://doi.org/10.1149/2.F03113IF.

(36) Wandt, J.; Freiberg, A.; Thomas, R.; Gorlin, Y.; Siebel, A.; Jung, R.; Gasteiger, H. A.; Tromp, M. Transition Metal Dissolution and Deposition in Li-Ion Batteries Investigated by Operando X-Ray Absorption Spectroscopy. *J Mater Chem A Mater* **2016**, *4* (47), 18300–18305. https://doi.org/10.1039/C6TA08865A.

(37) Fears, T. M.; Doucet, M.; Browning, J. F.; Baldwin, J. K. S.; Winiarz, J. G.; Kaiser, H.; Taub, H.; Sacci, R. L.; Veith, G. M. Evaluating the Solid Electrolyte Interphase Formed on Silicon Electrodes: A Comparison of Ex Situ X-Ray Photoelectron Spectroscopy and in Situ Neutron Reflectometry. *Physical Chemistry Chemical Physics* **2016**, *18* (20), 13927–13940. https://doi.org/10.1039/C6CP00978F.

(38) Bridges, C. A.; Sun, X. G.; Zhao, J.; Paranthaman, M. P.; Dai, S. In Situ Observation of Solid Electrolyte Interphase Formation in Ordered Mesoporous Hard Carbon by Small-Angle Neutron Scattering. *Journal of Physical Chemistry C* **2012**, *116* (14), 7701–7711. https://doi.org/10.1021/JP3012393.

(39) Kawaura, H.; Harada, M.; Kondo, Y.; Kondo, H.; Suganuma, Y.; Takahashi, N.; Sugiyama, J.; Seno, Y.; Yamada, N. L. Operando Measurement of Solid Electrolyte Interphase Formation

at Working Electrode of Li-Ion Battery by Time-Slicing Neutron Reflectometry. *ACS Appl Mater Interfaces* **2016**, *8* (15), 9540–9544. https://doi.org/10.1021/ACSAMI.6B01170.

(40) Jones, E. M. C.; Çapraz, Ö. Ö.; White, S. R.; Sottos, N. R. Reversible and Irreversible Deformation Mechanisms of Composite Graphite Electrodes in Lithium-Ion Batteries. *J. Electrochem. Soc.* **2016**, *163* (9), A1965–A1974. https://doi.org/10.1149/2.0751609jes.

(41) Gribble, D. A.; Li, Z.; Ozdogru, B.; McCulfor, E.; Çapraz, Ö.; Pol, V. G. Mechanistic Elucidation of Electronically Conductive PEDOT:PSS Tailored Binder for a Potassium-Ion Battery Graphite Anode: Electrochemical, Mechanical, and Thermal Safety Aspects. *Adv Energy Mater* **2022**, *12* (14), 2103439. https://doi.org/10.1002/AENM.202103439.

(42) Özdogru, B.; Cha, Y.; Gwalani, B.; Murugesan, V.; Song, M. K.; Çapraz, Ö. Ö. In Situ Probing Potassium-Ion Intercalation-Induced Amorphization in Crystalline Iron Phosphate Cathode Materials. *Nano Lett* **2021**, *21* (18), 7579–7586. https://doi.org/10.1021/ACS.NANOLETT.1C02095.

(43) Çapraz; Rajput, S.; White, S.; Sottos, N. R. Strain Evolution in Lithium Manganese Oxide Electrodes. *Exp Mech* **2018**, *58* (4), 561–571. https://doi.org/10.1007/S11340-018-0381-8/.

(44) Ramana, C. v.; Mauger, A.; Gendron, F.; Julien, C. M.; Zaghib, K. Study of the Li-Insertion/Extraction Process in LiFePO4/FePO4. *J Power Sources* **2009**, *187* (2), 555–564. https://doi.org/10.1016/J.JPOWSOUR.2008.11.042.

(45) Li, D.; Zhou, H. Two-Phase Transition of Li-Intercalation Compounds in Li-Ion Batteries. *Materials Today* **2014**, *17* (9), 451–463. https://doi.org/10.1016/J.MATTOD.2014.06.002.

(46) Laffont, L.; Delacourt, C.; Gibot, P.; Wu, M. Y.; Kooyman, P.; Masquelier, C.; Tarascon, J. M. Study of the LiFePO4/FePO4two-Phase System by High-Resolution Electron Energy Loss Spectroscopy. *Chemistry of Materials* **2006**, *18* (23), 5520–5529. https://doi.org/10.1021/CM0617182.

(47) Özdogru, B.; Koohbor, B.; Çapraz, Ö. Ö. The Impact of Alkali-Ion Intercalation on Redox Chemistry and Mechanical Deformations: Case Study on Intercalation of Li, Na, and K Ions into FePO4 Cathode. *Electrochemical Science Advances* **2022**, *2* (4), e2100106. https://doi.org/10.1002/ELSA.202100106.

(48) Ozdogru, B.; Murugesan, V.; Çapraz, Ö. Ö. Rate-Dependent Electrochemical Strain Generation in Composite Iron Phosphate Cathodes in Li-Ion Batteries. *J Mater Res* **2022**, *37* (19), 3237–3248. https://doi.org/10.1557/S43578-022-00649-4.

(49) Bassett, K. L.; Özgür Çapraz, Ö.; Özdogru, B.; Gewirth, A. A.; Sottos, N. R. Cathode/Electrolyte Interface-Dependent Changes in Stress and Strain in Lithium Iron Phosphate Composite Cathodes. *J Electrochem Soc* **2019**, *166* (12), A2707–A2714. https://doi.org/10.1149/2.1391912JES.

(50) Huang, H.; Yin, S. C.; Nazar, L. F. Approaching Theoretical Capacity of LiFePO4 at Room Temperature at High Rates. *Electrochemical and Solid-State Letters* **2001**, *4* (10). https://doi.org/10.1149/1.1396695.

(51) Wang, Z.; Lee, J. Z.; Xin, H. L.; Han, L.; Grillon, N.; Guy-Bouyssou, D.; Bouyssou, E.; Proust, M.; Meng, Y. S. Effects of Cathode Electrolyte Interfacial (CEI) Layer on Long Term Cycling of All-Solid-State Thin-Film Batteries. *J Power Sources* **2016**, *324*, 342–348. https://doi.org/10.1016/j.jpowsour.2016.05.098.

(52) Steinhauer, M.; Risse, S.; Wagner, N.; Friedrich, K. A. Investigation of the Solid Electrolyte Interphase Formation at Graphite Anodes in Lithium-Ion Batteries with Electrochemical Impedance Spectroscopy. *Electrochim Acta* **2017**, *228*, 652–658. https://doi.org/10.1016/J.ELECTACTA.2017.01.128.

(53) Louli, A. J.; Eldesoky, A.; deGooyer, J.; Coon, M.; Aiken, C. P.; Simunovic, Z.; Metzger, M.; Dahn, J. R.; Louli, A. J.; Eldesoky, A.; deGooyer, J.; Coon, M.; Aiken, C. P.; Simunovic, Z.; Metzger, M.; Dahn, J. R. Different Positive Electrodes for Anode-Free Lithium Metal Cells. *JElS* **2022**, *169* (4), 040517. https://doi.org/10.1149/1945-7111/AC62C4.

(54) Betz, J.; Brinkmann, J. P.; Nölle, R.; Lürenbaum, C.; Kolek, M.; Stan, M. C.; Winter, M.; Placke, T. Cross Talk between Transition Metal Cathode and Li Metal Anode: Unraveling Its Influence on the Deposition/Dissolution Behavior and Morphology of Lithium. *Adv Energy Mater* **2019**, *9* (21), 1900574. https://doi.org/10.1002/AENM.201900574.

(55) Portalis, G.; Carrapa, E.; Simon, B.; Vivier, V. Electrochemical Impedance Spectroscopy Investigation on Battery Materials Using a Symmetrical Cell. *Journal of Solid State Electrochemistry* **2021**, *25* (6), 1915–1926. https://doi.org/10.1007/S10008-021-04962-6.

(56) Liu, Y.; Xie, J. Failure Study of Commercial LiFePO $_4$ Cells in Overcharge Conditions Using Electrochemical Impedance Spectroscopy. *J Electrochem Soc* **2015**, *162* (10), A2208–A2217. https://doi.org/10.1149/2.0911510jes.

(57) Qian, Y.; Niehoff, P.; Börner, M.; Grützke, M.; Mönnighoff, X.; Behrends, P.; Nowak, S.; Winter, M.; Schappacher, F. M. Influence of Electrolyte Additives on the Cathode Electrolyte Interphase (CEI) Formation on LiNi1/3Mn1/3Co1/3O2 in Half Cells with Li Metal Counter Electrode. *J Power Sources* **2016**, *329*, 31–40. https://doi.org/10.1016/J.JPOWSOUR.2016.08.023.

(58) Kim, T.; Choi, W.; Shin, H. C.; Choi, J. Y.; Kim, J. M.; Park, M. S.; Yoon, W. S. Applications of Voltammetry in Lithium Ion Battery Research. *Journal of Electrochemical Science and Technology* **2020**, *11* (1), 14–25. https://doi.org/10.33961/JECST.2019.00619.

(59) Smith, A. J.; Burns, J. C.; Zhao, X.; Xiong, D.; Dahn, J. R. A High Precision Coulometry Study of the SEI Growth in Li/Graphite Cells. *J Electrochem Soc* **2011**, *158* (5), A447. https://doi.org/10.1149/1.3557892.

(60) Ellis, L. D.; Allen, J. P.; Hill, I. G.; Dahn, J. R. High-Precision Coulometry Studies of the Impact of Temperature and Time on SEI Formation in Li-Ion Cells. *J Electrochem Soc* **2018**, *165* (7), A1529–A1536. https://doi.org/10.1149/2.1091807JES.

(61) Özdogru, B.; Dykes, H.; Gregory, D.; Saurel, D.; Murugesan, V.; Casas-Cabanas, M.; Çapraz, Ö. Elucidating Cycling Rate-Dependent Electrochemical Strains in Sodium Iron Phosphate Cathodes for Na-Ion Batteries. *J Power Sources* **2021**, *507*. https://doi.org/10.1016/j.jpowsour.2021.230297.

(62) Malmgren, S.; Ciosek, K.; Hahlin, M.; Gustafsson, T.; Gorgoi, M.; Rensmo, H.; Edström, K. Comparing Anode and Cathode Electrode/Electrolyte Interface Composition and Morphology Using Soft and Hard X-Ray Photoelectron Spectroscopy. *Electrochim Acta* **2013**, *97*, 23–32. https://doi.org/10.1016/J.ELECTACTA.2013.03.010.

(63) Lee, H.; Lim, H. S.; Ren, X.; Yu, L.; Engelhard, M. H.; Han, K. S.; Lee, J.; Kim, H. T.; Xiao, J.; Liu, J.; Xu, W.; Zhang, J. G. Detrimental Effects of Chemical Crossover from the Lithium Anode to Cathode in Rechargeable Lithium Metal Batteries. *ACS Energy Lett* **2018**, *3* (12), 2921–2930. https://doi.org/10.1021/ACSENERGYLETT.8B01819.

(64) Browning, J. F.; Baggetto, L.; Jungjohann, K. L.; Wang, Y.; Tenhaeff, W. E.; Keum, J. K.; Wood, D. L.; Veith, G. M. In Situ Determination of the Liquid/Solid Interface Thickness and Composition for the Li Ion Cathode LiMn1.5Ni0.5O4. *ACS Appl Mater Interfaces* **2014**, *6* (21), 18569–18576. https://doi.org/10.1021/AM5032055.

(65) Moshkovich, M.; Cojocaru, M.; Gottlieb, H. E.; Aurbach, D. *The Study of the Anodic Stability of Alkyl Carbonate Solutions by in Situ FTIR Spectroscopy, EQCM, NMR and MS*; 2001; Vol. 497.

(66) Su, C. C.; He, M.; Amine, R.; Chen, Z.; Sahore, R.; Dietz Rago, N.; Amine, K. Cyclic Carbonate for Highly Stable Cycling of High Voltage Lithium Metal Batteries. *Energy Storage Mater* **2019**, *17*, 284–292. https://doi.org/10.1016/J.ENSM.2018.11.003.

(67) Guéguen, A.; Streich, D.; He, M.; Mendez, M.; Chesneau, F. F.; Novák, P.; Berg, E. J. Decomposition of LiPF 6 in High Energy Lithium-Ion Batteries Studied with Online Electrochemical Mass Spectrometry . *J Electrochem Soc* **2016**, *163* (6), A1095–A1100. https://doi.org/10.1149/2.0981606JES.

(68) Çapraz, Ö. Ö.; Bassett, K. L.; Gewirth, A. A.; Sottos, N. R. Electrochemical Stiffness Changes in Lithium Manganese Oxide Electrodes. *Adv Energy Mater* **2017**, *7* (7), 1601778. https://doi.org/10.1002/AENM.201601778.

(69) Browning, K. L.; Baggetto, L.; Unocic, R. R.; Dudney, N. J.; Veith, G. M. Gas Evolution from Cathode Materials: A Pathway to Solvent Decomposition Concomitant to SEI Formation. *J Power Sources* **2013**, *239*, 341–346. https://doi.org/10.1016/j.jpowsour.2013.03.118.